Biophysical Chemistry 27 (1987) 149–172
Elsevier

BPC 01166

Theory of electric dissipative structure in Characean internode

Kiyoshi Toko [a], Takanori Fujiyoshi [a], Koreaki Ogata [b], Hiroyuki Chosa [a] and Kaoru Yamafuji [a]

[a] *Department of Electronics, Faculty of Engineering, Kyushu University 36, Fukuoka 812* and [b] *Department of Physiology, College of Medical Technology Kansai, Amagasaki 660, Hyougo, Japan*

Received 18 May 1986
Revised manuscript received 6 September 1986
Accepted 14 February 1987

Dissipative structure; Band formation; Vacuole; Diffusion; Kinetics; (*Chara*)

A band-type alternating pattern of acidic and alkaline regions formed along the Characean cell wall is discussed theoretically. The model system is constructed from linear diffusion equations for the concentration of H^+ outside the internode and in the protoplasm. The plasmalemma is taken as a boundary transporting H^+ under energy supply by light. The sizes of the protoplasm and extracellular water phase are taken into account explicitly in the present model system to reproduce qualitatively the characteristics observed in various types of experiments. Theoretical analysis shows that the band pattern belongs to dissipative structures emerging far from equilibrium, and is stabilized through the electric current loops produced by locally activated electrogenic H^+ pumps and spatially separated passive H^+ influx (or OH^- efflux) across the membrane. Both the numerical calculation and the theoretical analysis using a generalized time-dependent Ginzburg-Landau equation reveal the following points: (i) the internodal cell with a larger vacuole in a smaller size of the extracellular water phase tends to exhibit a clearer band pattern; (ii) the increase in viscosity of the external aqueous medium makes the bands appear more easily and, furthermore, distinctly; (iii) the change in size of the extracellular water phase significantly affects the kinetics of the pattern-formation process. These results are interpreted reasonably by taking account of the electric current circulating between the acidic and alkaline regions.

1. Introduction

Characean species such as *Nitella* and *Chara* develop acidic and alkaline regions along their cell walls under illumination. The electric properties such as the electric potential near the cell wall, membrane potential and membrane conductance also show similar spatial patterns [1–5]. A light intensity exceeding some threshold value is necessary for the appearance of patterns. H^+ efflux (or equivalent OH^- influx) occurs in the acidic zones with H^+ influx (or OH^- efflux) in the alkaline zones. An electric current composed of H^+, therefore, may flow from the acidic to alkaline zones subject to the electrochemical gradient. Although the band pattern of these regions exists stably under normal conditions, it can sometimes be altered when the ammonia, methylamine or $CaCO_3$ concentration is changed, or when cyclosis is inhibited [6,7]. These facts may suggest that the spatial pattern is brought about by the localized activation of H^+-ATPase molecules playing the role of H^+ pumps distributed homogeneously within the cell membrane.

Recently, Toko and Yamafuji [8–10] proposed a theoretical model for explaining the banding phenomena in Characean cells. It was revealed that the band belongs to a dissipative structure appearing far from equilibrium [11]: The alternating acidic and alkaline regions are stabilized

Correspondence address: K. Toko, Department of Electronics, Faculty of Engineering, Kyushu University 36, Fukuoka 812, Japan.

0301-4622/87/$03.50 © 1987 Elsevier Science Publishers B.V. (Biomedical Division)

through the electric current loops produced by the locally activated H^+ pumps associated with spatially separated passive H^+ influx (or OH^- efflux) across the membrane. The banding state, where a longitudinal axial symmetry is broken with the circumferential symmetry being retained, was shown to be characteristic of an ion-transport system with a cylindrical shape. We can therefore term this new state appearing under illumination an 'electric dissipative structure' in the sense that it is accompanied by a circulating electric current around the cell or cells. According to this conclusion, we performed experiments in a unicellular system such as *Acetabularia* and a multicellular system like bean root [9,10,12]. As expected [13], periodic localization of chloroplasts in the form of transverse bands was found in the stalk of *Acetabularia* in Ca^{2+}-rich seawater. Furthermore, banding of pH and electric potential near the surface was observed in azuki beans (*Phaseolus chrysanthos*).

The model proposed previously [8] could describe well many typical tendencies of the observed data in Characean internodal cells, i.e., the appearance of bands beyond the critical light intensity, greater numbers of bands for higher light intensity, an M-shaped flux pattern at the membrane, etc. Furthermore, the high pH value in the alkaline regions was explained by considering the H^+ circulation due to H^+ pumps and passive influx without assuming the existence of OH^- pumps. In the present paper, we describe the other basic quantitative data such as the light intensity and diffusion constant of the extracellular medium, including the pH values.

Another purpose of the present work is also to stress the nonequilibrium properties of the banding: The system concerned exhibits an electric current circuit in the cytoplasm and the external aqueous solution [2,8–10]. This may enable us to expect that the changes in volumes of these regions can significantly affect the typical properties in banding phenomena, since the flow pattern can be markedly altered. So far, however, no study has been made concerning the effect of the volume of the reservoir containing the cell, i.e., that of the extracellular water phase on the banding. This may originate partly from the lack of recognition that the bands are rather a dynamic structure corresponding to a self-organized state, existing under far-from-equilibrium conditions. In the present paper, therefore, we adopt a slightly modified model in which the sizes of the extracellular water phase and vacuole are taken into account explicitly. Properties such as alkalinization and the dynamics of pattern formation are studied based on this model. The experimental results obtained using a water-film electrode [4,5] on the kinetics of band formation are described in the accompanying paper [14].

2. A theoretical model

Fig. 1 illustrates a situation where a Characean internode exhibits a band-type flux pattern under illumination. A model system is shown in fig. 2a: An internode of radius R lies between $z = L_1$ and L_2 surrounded by the external aqueous solution, the size being given by radius R_r and length L_r. The vacuole occupies the region $0 \leqq r \leqq R_v$ and $L_{1v} \leqq z \leqq L_{2v}$. Since the band pattern can appear prior to any pattern with breaking of circumferential symmetry [9], the angular dependence is not taken into account here. The protoplasm exists in the slit bounded by $r = R_v$ and $r = R$ containing the region $L_1 \leqq z \leqq L_{1v}$ and $L_{2v} \leqq z \leqq L_2$. We assume H^+ circulation occurs in the protoplasm and the external medium.

2.1. Diffusion equation and H^+ flux

If the H^+ concentration is represented by $n(r, z, t)$ with t denoting the time, the diffusion equations in the external environment and the protoplasm are given by

$$\frac{\partial n}{\partial t} = \begin{cases} D_e\left[\frac{1}{r}\frac{\partial}{\partial r}\left(r\frac{\partial}{\partial r}\right) + \frac{\partial^2}{\partial z^2}\right]n & \text{in the external solution,} \\ D_i\left[\frac{1}{r}\frac{\partial}{\partial r}\left(r\frac{\partial}{\partial r}\right) + \frac{\partial^2}{\partial z^2}\right]n & \text{in the protoplasm,} \end{cases} \quad (1)$$

where D_e and D_i are the diffusion constants of protons in the external solution and protoplasm,

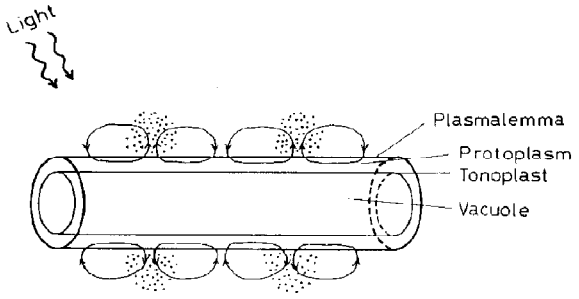

Fig. 1. Schematic illustration of Characean banding accompanied by a circulating electric current.

respectively. A nonlinear driving term caused by the electric potential gradient is omitted in eq. 1 because of its negligibly small value [8,9,15]. This term is also disregarded below for the same reason. All quantities appearing in eq. 1 and also introduced hereafter are normalized as nondimensional (see appendix A).

Let us next provide expressions for an active flux, J_a, and a passive flux, J_p. The active flux J_a may originate in the activation of H^+-ATPase molecules within the membrane at $r = R$; we adopt the following nonlinear function of internal variables h and Δn based on a statistical average [8]:

$$J_a = \frac{\alpha}{1 + \exp[(h - \Delta n)/\gamma]}, \tag{2}$$

with the numerical coefficient α denoting the maximum active-flux density of protons when all H^+-ATPase molecules are activated. Another numerical coefficient $1/\gamma$ represents the sharpness of the sigmoid curve as an increasing function of Δn.

The proton concentration difference across the membrane $\Delta n(z, t)$ is defined by

$$\Delta n = n_{es} - n_{is}, \tag{3}$$

with n_{es} and n_{is} denoting the values of the H^+ concentration $n(z, r, t)$ at the external ($r = R + 0$) and internal ($r = R - 0$) surfaces of plasmalemma, respectively. The sign of the flux is taken as plus for efflux. Eq. 2 implies the favourable activation of H^+-ATPase via the formation of an H^+-concentration difference. This is a kind of positive-feedback process, since the activation can build up the H^+-concentration difference. The existence of a positive-feedback route through HCO_3^- production is really indicated from a few experiments [16]. Furthermore, it may be possible that photosynthesis is activated more by the CO_2 influx at the acidic region, which leads to ATP production for the activation of H^+ pumps.

The internal variable h expresses an inhibitory factor for the pump activation: increasing h brings about a decrease in J_a. We assume that h is a function of the light intensity alone, independent

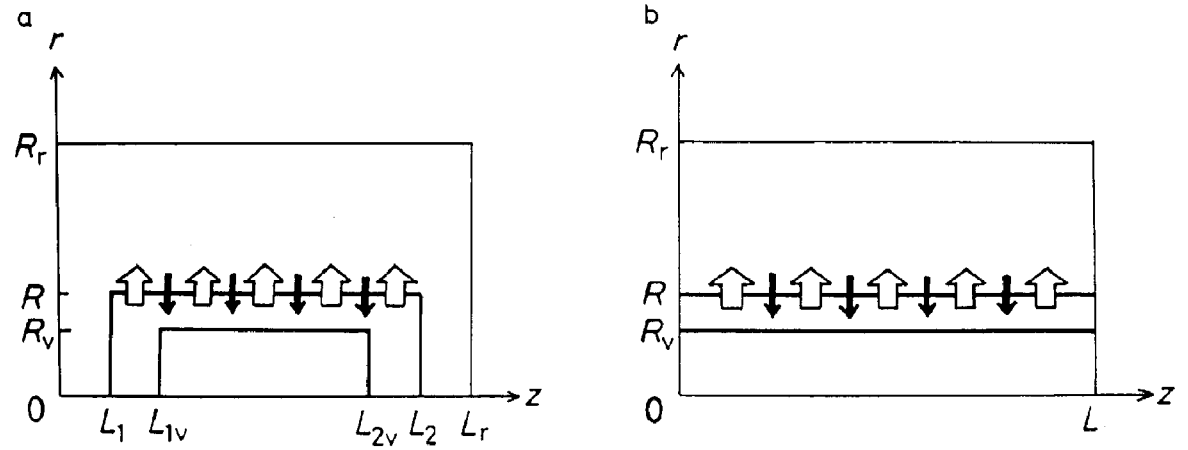

Fig. 2. Spatial coordinates for numerical calculation (a) and theoretical analysis (b). The reservoir size R_r and vacuole size R_v can be changeable. $R = 0.85$, $L = L_2 - L_1 = 50$, $L_r = 60$ and $L_v = L_{1v} - L_{2v} = 49$. Since the normalized factor $\tilde{R}$ is chosen as 0.05 cm, the above values imply an internodal cell of radius 0.425 mm and length 25 mm, which corresponds to the usual cell prepared for measurements.

of the spatial coordinates. ADP molecules act inhibitorily on the pump [17], and hence one candidate for the inhibitory factor may be considered as being ADP.

The present system is very far from equilibrium because of the continuous supply of light energy. While light may produce ATP as an energy source for H^+ pumps through complex chemical reactions with many steps, the detailed mechanism has not yet been clarified. At the present stage, therefore, we assume a simple relationship between the light intensity I and the inhibitory factor h. If the average active flux J_a^T is defined by

$$J_a^T = \frac{1}{L}\int_0^L J_a \, dz, \tag{4}$$

then J_a^T is expected to increase with the light intensity I as

$$J_a^T = aI, \tag{5}$$

where a is a numerical constant. The saturation effect of J_a^T is disregarded for much greater light intensity, since we are now interested in the behavior of a system where the patterned state has appeared as a consequence of the instability of the homogeneous-flux state with increasing light intensity. Eq. 5 states that the illumination with light activates H^+ efflux on average. As shown later, eq. 5 demonstrates the tendency of h decreasing when I is increased; this is reasonable because h concerns the inhibitory factor and light induces spatial inhomogeneity of the electric current through the activation of H^+-ATPase.

As for the passive flux J_p, we adopt the linear relation:

$$J_p = -p\Delta n, \tag{6}$$

where p denotes the permeability.

We must point out that J_a is not necessarily a nonlinear function as given by eq. 2 but that the total flux $J_a + J_p$ only has to show a nonlinear property. In fact, this kind of nonlinearity can be expected from the following suggestion [5,18]. The high pH is maintained by H^+ influx in the alkaline regions, which in itself is promoted by the high pH since the membrane in this state is highly permeable to H^+ (or OH^-). In this case, J_p may become rather nonlinear. However, the usual modification of J_p along this line is mathematically equivalent to the present eqs. 2 and 6, since a similar type of nonlinearity is only added in the present system.

2.2. Boundary conditions

The boundary condition on the cell membrane at $r = R$ is given by the flux continuity across the membrane as

$$-D_e\left(\frac{\partial n_e}{\partial r}\right)_s = -D_i\left(\frac{\partial n_i}{\partial r}\right)_s = J_a + J_p \text{ at } r = R, \tag{7}$$

where $(\partial n_e/\partial r)_s$ and $(\partial n_i/\partial r)_s$ designate the derivatives of $n(r,z,t)$ at the exterior $(r = R + 0)$ and interior $(r = R - 0)$ surfaces of the membrane, respectively.

The two ends of the cell are reasonably described as poorly permeable to H^+, since the boundary condition at the ends scarcely affects band formation [8], as has also been suggested experimentally [4]. Thus, we have

$$\partial n/\partial z = 0 \text{ at } z = L_1 \text{ and } L_2,\ 0 \leqq r \leqq R. \tag{8a}$$

The length of cell is

$$L = L_2 - L_1. \tag{9}$$

The condition at the tonoplast is assumed as that pertaining to no flux:

$$\partial n/\partial r = 0 \text{ at } r = R_v,\ L_{1v} \leqq z \leqq L_{2v},$$
$$\partial n/\partial z = 0 \text{ at } z = L_{1v} \text{ and } L_{2v},\ 0 \leqq r \leqq R_v. \tag{8b}$$

This may be somewhat crude, but it is necessary to put forward this condition as being one of the plausible conditions for the moment, since there exist no reliable data on the permeability of the tonoplast to H^+. It is well known in many plant species [19] that H^+-ATPase is contained in the tonoplast. The first step of acid/alkali pattern formation may originate in ion transport at the plasmalemma, as suggested from experimental data on the electric properties [1–7,14,18]. Therefore, H^+ transport across the tonoplast may act as a controllable factor of cellular homeostasis including energy coupling. This problem connected

with the spatial electric pattern is important and interesting, but will not be pursued further here; a theoretical description of H^+ transport at the plasmalemma with diffusion in the extracellular and intracellular spaces is made. Eq. 8b implies that H^+ may flow parallel to the tonoplast. It may not contradict the observation that protoplasmic streaming plays an important role in the bands [7], since the streaming in fact occurs parallel to the tonoplast. In our model the effect of vacuole size is incorporated purely in a physical way, i.e., the change in R_v, for which the boundary condition eq. 8b holds. The electric current can thus flow in the narrow region limited by R_v and R.

The boundary condition for the reservoir (i.e., extracellular water phase) is as follows:

$$\partial n/\partial r = 0 \text{ at } r = R_r,\ 0 \leqq z \leqq L_r,$$
$$\partial n/\partial z = 0 \text{ at } z = 0 \text{ and } L_r,\ 0 \leqq r \leqq R_r. \qquad (8c)$$

This condition means that the external aqueous solution is contained in a cylindrical vessel of radius R_r and length L_r. A decrease in R_r leads to a diminishing region where H^+ can flow. It can be expected to alter the flow-pattern characteristic of the system.

If eq. 1 is solved numerically under the conditions imposed by eqs. 7 and 8 with the integral constraints of eqs. 4 and 5, we can realize spatial patterns of H^+ flux as observed in the real situation (see figs. 3 and 4). For the analytical discussion, however, it is quite difficult to deal directly with the boundary conditions eqs. 8a–8c. We therefore simplify these conditions in order to analyze the characteristic properties more easily. Fig. 2b concerns the theoretical analysis: All the lengths of cell, vacuole and reservoir are set as equal to L. Thus, eqs. 8a–8c can be rewritten as

$$\partial n/\partial z = 0 \text{ at } z = 0 \text{ and } L,\ 0 \leqq r \leqq R_r,$$
$$\partial n/\partial r = 0 \text{ at } r = R_v \text{ and } R_r,\ 0 \leqq z \leqq L, \qquad (10)$$

Even this simplification will give a fairly good explanation of both the numerical and experimental results.

2.3. Properties of the present model system

The model system described above for a Characean cell immersed in an external aqueous solution has the following characteristics:

(i) The kinetic equations (eq. 1) holding in the cell exterior and protoplasm are linear differential equations.

(ii) The boundary condition eq. 7 with eqs. 2 and 6 is nonlinear and time-dependent.

(iii) The average active flux J_a^T is restricted by the light intensity I in eqs. 4 and 5.

(iv) The region where H^+ can flow is limited to the protoplasm at $R_v \leqq r \leqq R$ and the extracellular water phase at $R \leqq r \leqq R_r$.

It should be noted that only the nonlinearity, i.e., positive feedback, cannot produce a stable spatial pattern. The stabilization of the pattern requires another repressive factor, which is expressed by restriction of the overall activation of H^+ pumps along the cell.

The usual theories of pattern formation concern only the interior of a unicellular or multicellular system [11,20]. The present model, on the other hand, immediately takes account of the membrane separating the cell interior from the exterior. This type of problem is rather analogous to an oligomeric model [21], where a two-dimensional diffusion occurs over the membrane surface with a nonlinear transport process, while the mathematical description is much different.

3. Numerical results

In this section we describe the results of computer simulation, using an A.D.I. method [22].

3.1. Electric dissipative structure

Fig. 3 demonstrates examples of a homogeneous-flux state (a) and band-patterned states (b and c), constructed from acid regions and alkaline regions. The numerical parameters adopted are listed in the figure legend. In each figure, the patterns of pH along the cell surface, active flux, passive flux and total flux as the sum of these two fluxes at the membrane are shown. The contour lines of H^+ concentration in the cell exterior are also drawn. The high pH value reaching about 9.0 occurs in the region where the H^+ flux enters, in accord with the usual observations [2,6,23].

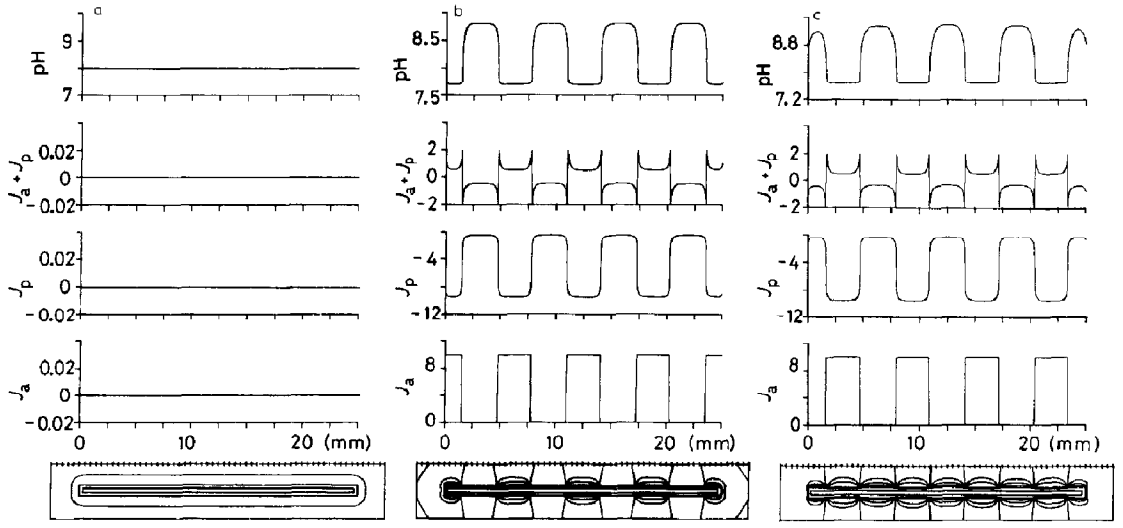

Fig. 3. Numerical results for the homogeneous-flux state (a) and patterned states (b and c). The pH values refer to those at the cell surface. The initial extracellular pH is chosen as 8.0. The contour lines with a step size of 0.02 are drawn at the bottom constructed from an internode and the external aqueous solution. (a) $I = 0.6$ W/m^2 and (b) $I = 24$ W/m^2 with $\alpha = 10$, $p = 4.8$, $\gamma = 0.12$, $D_e = 0.5$ ($= 10^{-4}$ cm^2/s), $D_i = 500$, $a = 0.2$ m^2/W, $R_v = 0.25$ mm, $R_r = 2.5$ mm, $n_\infty = 1.16 \times 10^{-8}$ M and $\tilde{n} = 0.141$. (c) $I = 24$ W/m^2 with $\gamma = 0.1$, $D_i = 1000$, $n_\infty = 1.09 \times 10^{-8}$ M, $\tilde{n} = 0.79$ and the same parameter values as in (a). The alkaline region is formed far from the node (b) and at the node (c). Whether each type of pattern appears depends on the imposed initial condition.

While the homogeneous-flux state can be obtained experimentally for a light intensity lower than about 0.8 W/m^2, the inhomogeneous state (patterned state) can arise from the homogeneous state when the light intensity is increased [3]. This observation is surely explained by the present numerical calculation: The patterned state appears spontaneously beyond the critical light intensity of approx. 0.8 W/m^2. The theoretical analysis detailed below reveals that the appearance of a patterned state corresponds to a bifurcation phenomenon [11] brought about by instability of the homogeneous state: A new ordered state of bands bifurcates from the homogeneous state. Increasing light intensity shifts the system far from equilibrium, so that the self-organized state such as banding can occur.

The numerical results on the flux display the typical M-shaped pattern. This explains the experimental observation [23] and demonstrates the circulation of H^+ flux from the acidic to alkaline region. Fig. 4 shows the streamline drawn so as to cross perpendicularly the contour lines of H^+ concentration. The streamline suggested from the measurement of surface electric potential [2] also shows a similar pattern.

In this way we can reproduce well banding phenomena in the Characeae within the framework of a simple theoretical model. Electric spatial patterns are formed mainly according to the H^+ (or OH^-) concentration pattern. The electric dissipative structure can be considered to appear frequently in many biological systems such as *Acetabularia* [9], bean root [10,12] and *Fucus* [24].

3.2. *The pH value at the surface*

Here, we describe the effects of the value of the diffusion constant in the protoplasm, and the sizes of the vacuole and reservoir on the pH value at the surface of cell when alternating acidic and alkaline regions are formed.

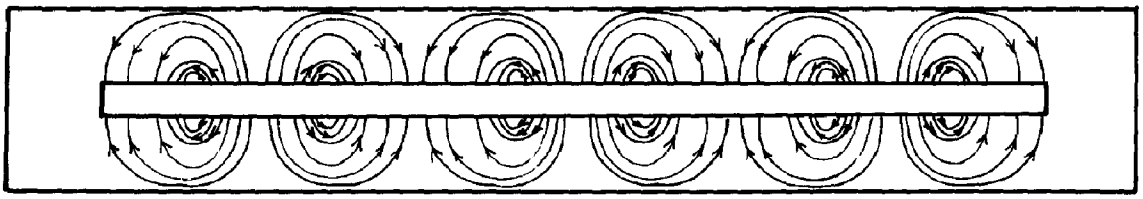

Fig. 4. The H^+ flux pattern drawn according to the contour lines. The vessel is assumed as being impermeable to H^+ at its wall.

Fig. 5 shows the relationship between D_i and the pH values of alkaline and acidic regions. The pH values are estimated at the midpoints of the alkaline and acidic regions. It can be seen that, when the value of D_i is increased, alkalinization is facilitated. If the velocity of H^+ streaming v is defined by the following equation:

$$v = D_i(\partial n/\partial z)/n, \tag{11}$$

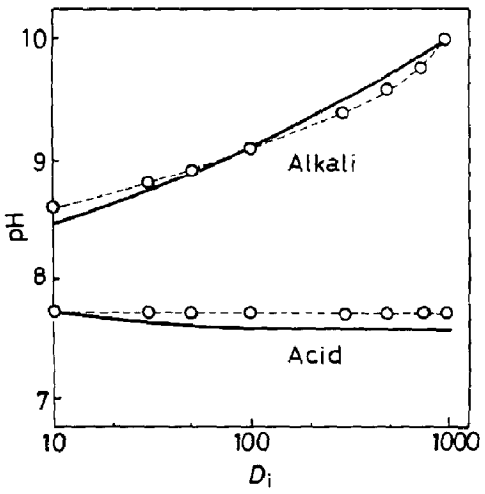

Fig. 5. Dependence of the pH values at the cell surface on the internal diffusion constant D_i. (O------O) Numerical results; conditions: $I = 12$ W/m^2 with $\alpha = 5$, $p = 2.4$, $\gamma = 0.01$, $D_e = 10^{-4}$ cm^2/s, $a = 0.2$ m^2/W, $R_v = 0$, $R_r = 2.5$ mm, $n_\infty = 1.23 \times 10^{-8}$ M and $\bar{n} = 0.18$. (———) Analytical results; conditions: $I = 4$ W/m^2 and $\alpha = 2$, $p = 1$, $\gamma = 0.1$, $D_e = 10^{-4}$ cm^2/s, $a = 0.2$ m^2/W, $R_v = 0.4$ mm, $R_r = 0.75$ mm, $n_\infty = 1.57 \times 10^{-8}$ M and $\bar{n} = 0.362$. While the parameter values in the theoretical analysis differ from those in the numerical analysis, it is because a reliable theoretical description is limited to a region near the critical light intensity showing relatively weak nonlinearity. Note that the TDGL equation can be derived near the homogeneous-flux state.

then the present computer simulation gives about 93 μm/s as the value of v near the midpoints of the acidic and alkaline zones for $D_i = 200$. This value is of the same order as the velocity of protoplasmic streaming suggested experimentally as 60–100 μm/s. The external diffusion constant D_e is, on the other hand, chosen as 0.5 ($= 10^{-4}$ cm^2/s), equal to the H^+ diffusion constant. The fact that D_i should be chosen as much larger than D_e to obtain the band pattern in the observed pH range might suggest the intervention of protoplasmic streaming.

The effect of vacuole size on the pattern is shown in fig. 6. The radius of the internode is chosen as 0.425 mm, in good agreement with the real radius of an internode. The larger the vacuole becomes, the more distinct the alkalinization appears. This result may explain the report that bands composed of acid and alkaline regions become obscure when the vacuole is removed [25]. We shall provide a reasonable interpretation of this phenomenon later.

Fig. 7 reveals that the reduction in reservoir (extracellular water phase) size makes the band pattern clearer. For a smaller size of vessel, the H^+ current is forced to flow in the narrow region parallel to the cell surface; thus, a sharp spatial variation of H^+ concentration is built up in the vicinity of the cell surface. We next show that this gives rise to the stabilization of a band pattern.

3.3. Dynamics of pattern formation

Fig. 8 visualizes the appearance of a band pattern when the light intensity is abruptly increased; the H^+ concentrations in the cell exterior and interior are illustrated. An overall increase in H^+ concentration along the cell surface occurs

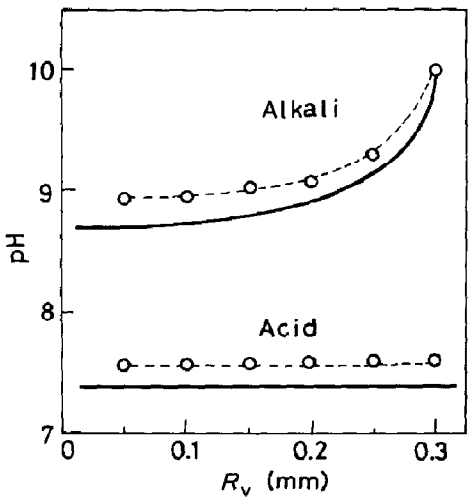

Fig. 6. Dependence of the surface pH values on the vacuole size R_v. The numerical results (O------O) adopt the parameter values used in fig. 3c. The theoretical analysis (———) adopts the same values as in fig. 5 except for $D_i = 1000$, $n_\infty = 1.895 \times 10^{-8}$ M, $\bar{n} = 0.4723$ and R_v changeable.

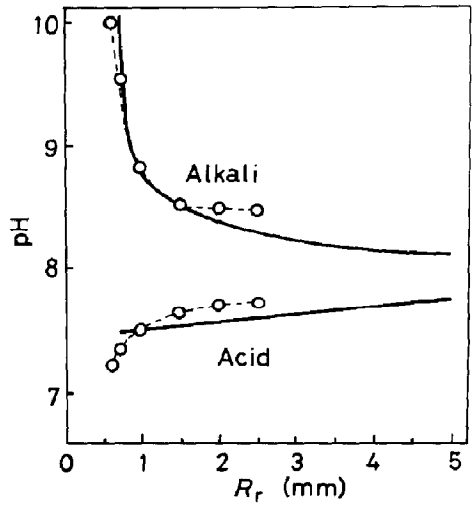

Fig. 7. Dependence of the surface pH values on the reservoir (extracellular water phase) size R_r. The numerical results (O------O) are obtained under the conditions: $I = 4$ W/m^2 with $\alpha = 2$, $p = 0.8$, $\gamma = 0.1$, $D_e = 2$ ($= 4 \times 10^{-4}$ cm^2/s), $D_i = 1000$, $R_v = 0.25$ mm, $R_r = 2.5$ mm, $n_\infty = 1.02 \times 10^{-8}$ M and $\bar{n} = 0.022$. The theoretical analysis (———) is due to the same parameter values as in fig. 5 except for $R_v = 0.4$ mm and R_r changeable.

first, but thereafter, localized accumulation of H^+ commences. At this stage, however, the H^+-concentration change extends over only the cell surface. It is associated with H^+ circulation along the surface. The alternating acid and alkaline regions are formed only near the cell surface. Later, the cell exterior exhibits the spatial pattern of H^+ concentration, which leads to a circulating electric current in the reservoir. This pattern in a system composed of a cell membrane, cell interior and exterior is realized according to the principle of minimum energy dissipation or minimum entropy production of the whole system [8].

Fig. 9 shows the time courses of pH values at the alkaline and acidic regions when the light intensity is abruptly raised and then reduced. A high alkaline value is formed for increasing light intensity but gradually disappears as the light is switched off. Since a circulating electric current is established around the cell, the dynamics of pattern formation can be expected to be greatly altered with change in reservoir size of the extracellular water phase.

Let us define the relaxation time $\tau\uparrow$ as the time required for the change of $(1 - e^{-1})$ times as the total change in flux at the alkaline region when the light intensity is raised. As for $\tau\downarrow$, the relaxation time with decreasing light intensity, it may be convenient to define it as the time for reaching the first concave peak of flux, because the relaxation process is oscillatory. The relations between the relaxation time and reservoir size are summarized in fig. 10: When a band pattern is formed, relaxation is faster for the smaller vessel. When the homogeneous-flux state is recovered, on the other hand, the relaxation is slower for the smaller vessel. This indicates that the smaller vessel stabilizes the band state. This is because the acid and alkaline bands can be formed more readily for a smaller volume of water, as shown in fig. 7. These facts also imply that the banding phenomenon should be understood as a rather macroscopic phenomenon appearing not only in the cell interior but also in the exterior.

It is necessary to understand this phenomenon from a comparison with the fluid or reaction-diffusion system. In Benard convection, thermal energy supplied externally is consumed by homoge-

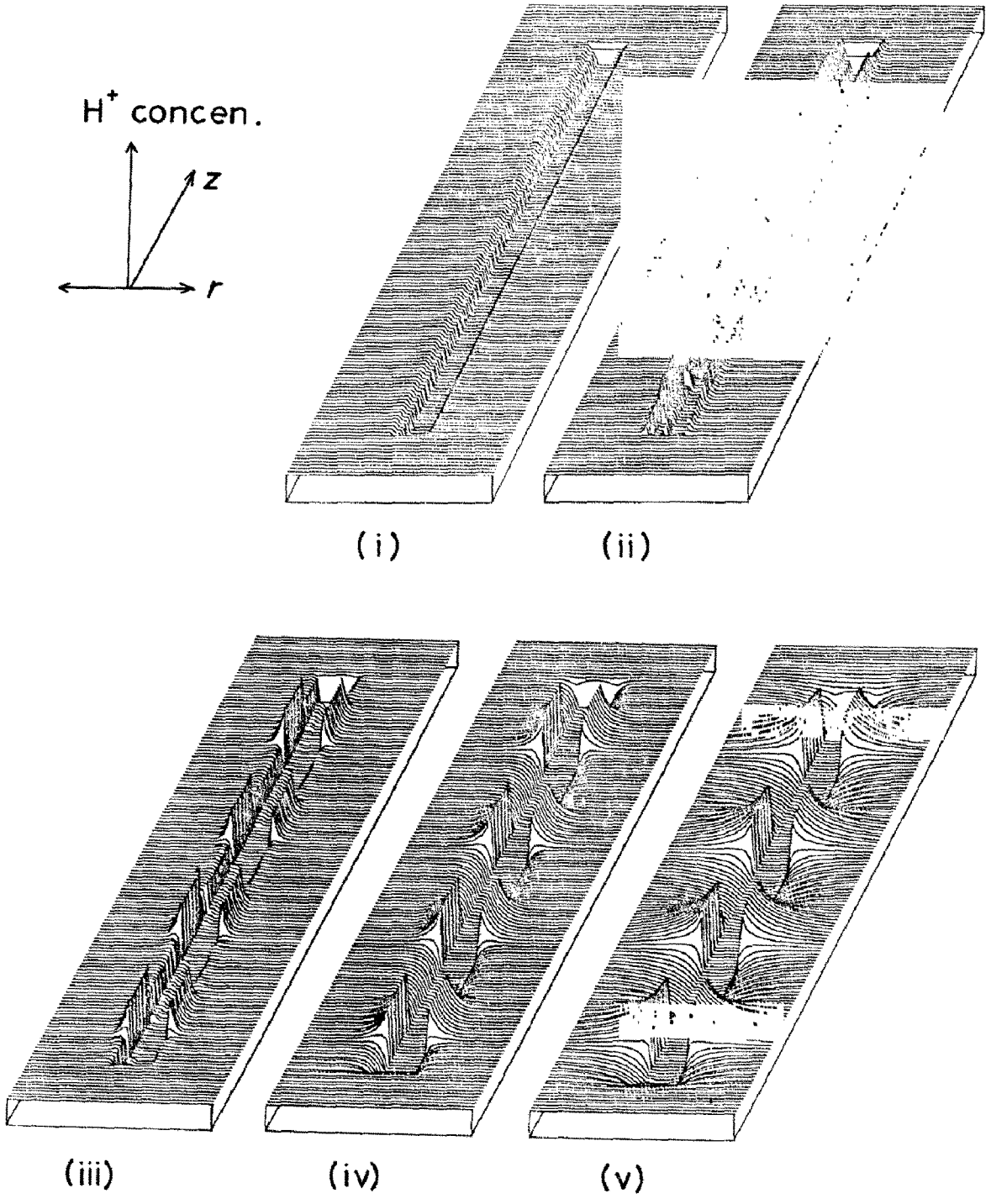

Fig. 8. Formation of the H^+ concentration gradient under the condition $I = 24$ W/m^2. The internodal cell is located in a central position, where the H^+ concentration is relatively low. Parameters are $\alpha = 12$, $D_i = 500$ and the same as those in fig. 3c. (i) Initial homogeneous-flux state. On illumination, the pattern gradually appears with time: (ii) $t = 0.25$ s, (iii) $t = 1.25$ s, (iv) $t = 6.25$ s and (v) $t = 50$ s.

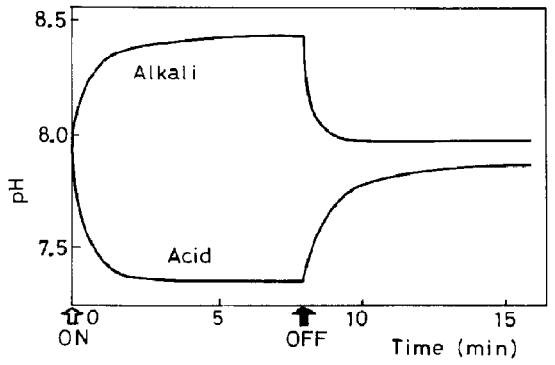

Fig. 9. Time courses of the rise and subsequent decline in pH values. The pH value in each region is estimated at the midpoint of that region. The parameter values are the same as those in fig. 7 except for $R_r = 2.5$ mm. At $t = 0$ (ON), a light intensity of 4 W/m^2 is imposed and at $t = 8$ min (OFF) it is decreased to 0.1 W/m^2.

neous conduction if the thermal difference is relatively small. For a large thermal difference, however, energy consumption cannot be made sufficiently by conduction but by patterned convective flow. Similar situations also occur in such reaction-diffusion systems as the Belousov-Zhabotinskii reaction and Liesegang ring [11]. In Characean systems, the homogeneous-flux state forms an extremely sharp variation of H^+ concentration perpendicular to the whole cell surface. This large discontinuous change in H^+ concentration is obviously disadvantageous from the viewpoint of energy dissipation, as is also understood from the appearance of phase separation in equilibrium systems [26,27]. In the patterned state, however, the sharp variation is restricted to the acid and alkaline regions; hence, the transitional regions between them show only small variations in H^+ concentration. In this case protons can escape to neighboring regions along the surface. The system no longer needs to pump H^+ strongly along the entire cell surface. Only if H^+ is extruded from the acidic region can H^+ flow passively into the neighboring alkaline regions. Energy dissipation in an entire system composed of a membrane, cell interior and exterior behaving as dissipative media becomes lower when the patterned state is realized. This is analogous to Benard convection in fluid systems or phase separation in equilibrium systems.

4. Stability of the homogeneous-flux state

A stationary homogeneous state can be described using eqs. 1, 4 and 5 under the boundary

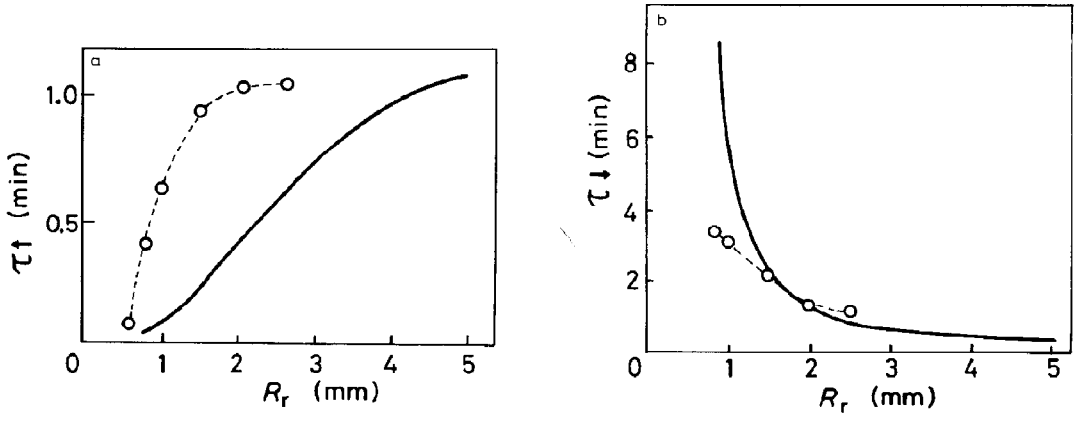

Fig. 10. Relationships between the reservoir size R_r and relaxation time to the patterned state (a) and homogeneous-flux state (b). The numerical (○------○) and theoretical (———) results are from the same parameter values as in fig. 7. Other parameters are $I' = 0$ and $b = 0.32$ W/m^2.

conditions of eqs. 7 and 10:

$$n^0 = \begin{cases} N_e = 1 + \dfrac{aI}{p}\dfrac{R^2 - R_v^2}{R_r^2 - R_v^2} & \text{at } R < r < R_r, \\ N_i = 1 - \dfrac{aI}{p}\dfrac{R_r^2 - R^2}{R_r^2 - R_v^2} & \text{at } R_v < r < R, \end{cases} \tag{12}$$

$$h^0 = \frac{aI}{p} + \gamma \ln\left[\frac{\alpha}{aI} - 1\right]. \tag{13}$$

Note that h^0 decreases with increase in light intensity I, as expected. The stationary H^+ concentration difference is given by

$$\Delta n^0 = N_e - N_i = aI/p, \tag{14}$$

which increases with I.

The stability of a homogeneous state is examined easily (details are given in appendix B). Fig. 11 depicts a phase diagram on the plane of L^{-2} and I. This diagram predicts that banding patterns appear easily for larger values of the light intensity I and cell length L. In fact, the bands can appear above the threshold value of light intensity of about 0.8 W/m^2 [3,4], and young cells of small length and cells shorter than a few millimeters are unable to maintain stable bands [18,28,29]. Fig. 11 also demonstrates that a spatial pattern with more bands can appear with light intensity. This explains the observation [3] and the computer simulation shown in fig. 3.

The critical light intensity I_c, above which the spatial pattern can appear, is given explicitly by

$$I_c = \left\{\alpha - \left(\alpha^2 - 4\gamma\alpha \times\left[p + \frac{k\pi}{L}\frac{D_e D_i X_c Y_c}{D_e Y_c Z_c - D_i X_c W_c}\right]\right)^{1/2}\right\}\Big/ 2a. \tag{15}$$

where k is an integer expressing the spatial mode: a pattern composed of one alkaline and one acid band corresponds to $k = 2$, two sets of bands corresponding to $k = 4$, and so on. An example of fig 3b is obtained for $k = 8$. In eq. 15 the abbreviated expressions X_c, Y_c, Z_c and W_c are used as

$$\begin{aligned} X_c &= K_1(r_v)I_1(r_s) - I_1(r_v)K_1(r_s), \\ Y_c &= K_1(r_r)I_1(r_s) - I_1(r_r)K_1(r_s), \\ Z_c &= K_1(r_v)I_0(r_s) + I_1(r_v)K_0(r_s), \\ W_c &= K_1(r_r)I_0(r_s) + I_1(r_r)K_0(r_s), \end{aligned} \tag{16}$$

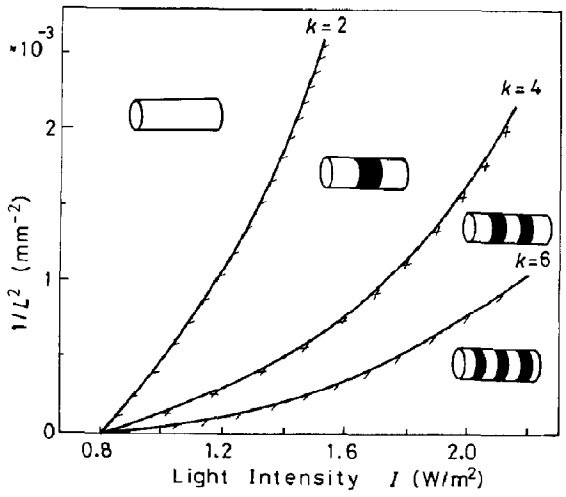

Fig. 11. Phase diagram on the plane of $1/L^2$ and I. The patterned state can appear more easily for the greater cell length L and higher light intensity I. The threshold above which the bands appear is nearly 0.8 W/m^2 for a sufficiently long internode. The parameters are $\alpha = 5000$, $p = 0.25$ ($= 10^{-3}$ cm/s), $\gamma = 0.15$, $D_e = 10^{-4}$ cm^2/s, $D_i = 200$, $a = 5$ m^2/W, $R_v = 0.4$ mm and $R_r = 2.5$ mm.

where $K_\nu(x)$ and $I_\nu(x)$ are modified Bessel functions of the ν-th order, and r_v, r_s and r_r are defined by

$$r_v = \frac{k\pi}{L}R_v, \quad r_s = \frac{k\pi}{L}R, \quad r_r = \frac{k\pi}{L}R_r. \tag{17}$$

Let us now discuss the effects of D_i, D_e, R_v and R_r on the bifurcation. Eq. 15 can be approximated by expanding the modified Bessel functions up to the first order:

$$2aI_c = \alpha - \left\{\alpha^2 - 4\gamma\alpha\left[p + \frac{k\pi}{2r_s L}\Big/ \left(\frac{1 - \frac{r_v^2}{2}\ln r_s}{D_i(r_s^2 - r_v^2)} + \frac{1 - \frac{r_r^2}{2}\ln r_s}{D_e(r_r^2 - r_s^2)}\right)\right]\right\}^{1/2}. \tag{18}$$

This expression shows that the bifurcation point,

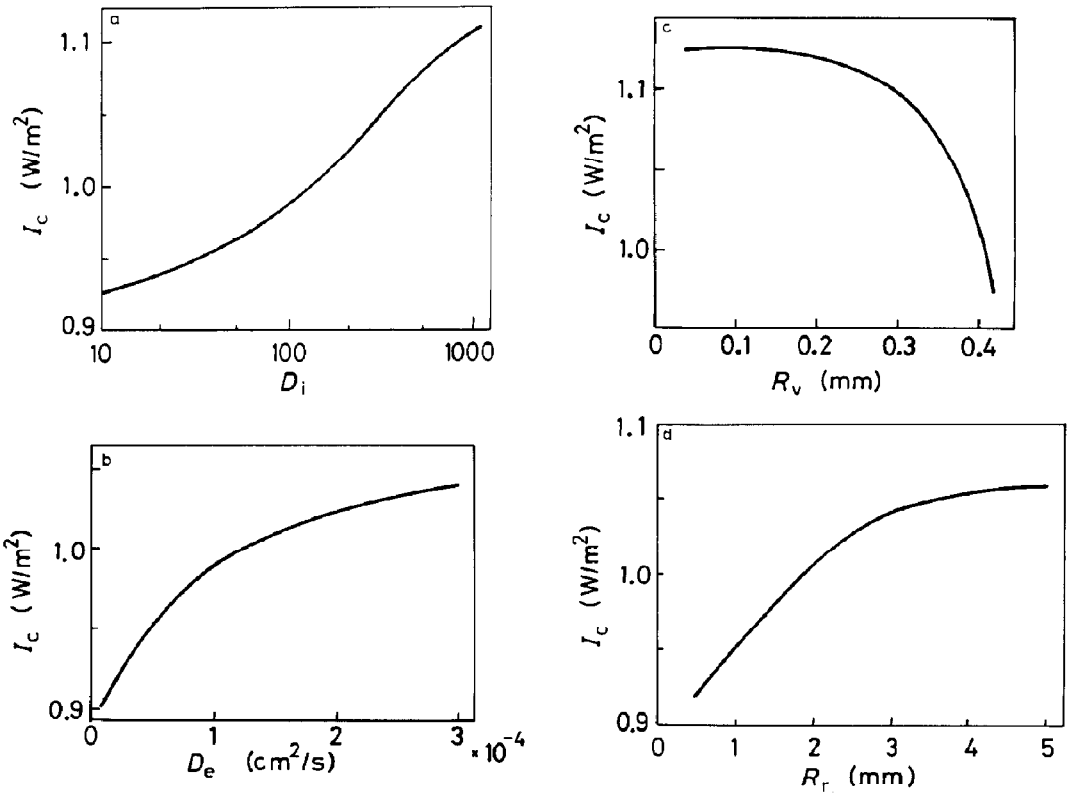

Fig. 12. Dependence of the critical light intensity I_c on the internal diffusion constant D_i (a), external diffusion constant D_e (b), vacuole size R_v (c) and reservoir size R_r (d). The parameters are $\alpha = 1$, $p = 1$, $D_e = 2 \times 10^{-4}$ cm^2/s, $a = 0.2$ m^2/W, and the same as those in fig. 11. One parameter value is changed in each panel.

i.e., the critical light intensity, increases with D_i or D_e. The appearance of a spatial pattern is delayed as the diffusion effect is dominant. This result does not conflict with the well-known role of diffusion in pattern formation [11]. The strict numerical results using eq. 15 are given in fig. 12a and b; the increase in diffusion constant produces a rise in I_c.

The effect of vacuole size is also studied using eq. 18. When the vacuole size is gradually decreased, I_c is known to increase. This means that the homogeneous-flux state is favorable when the vacuole is removed. This conclusion agrees qualitatively with the numerical results in fig. 6, and also explains the experimental observation [25]. The relation between vacuole size and critical light intensity is shown in fig. 12c.

The reservoir size can affect the bifurcation. When R_r is increased from nearly R, we can see from eq. 18 the rise in I_c. This means that band formation is advantageous for smaller sizes of the extracellular water phase and explains the kinetics obtained numerically shown in fig. 10. The bands are stable when the cell is in water with a smaller volume. Fig. 12d illustrates the relation between R_r and I_c calculated from eq. 15.

These results can be understood intuitively by taking into account fluctuation within the system. For the appearance of a self-organized state such as bands, the microscopic fluctuation appearing in the system must not decay but develop with time; macroscopic order is realized through fluctuations. When diffusion is fast, the fluctuation of concentration can be smoothed out straightforwardly

in the cell interior or exterior. The microscopic fluctuation, therefore, cannot develop into a macroscopic fluctuation, i.e., self-organized state. The system will remain in the homogeneous state. According to the theoretical result in fig. 12, however, the change in critical light intensity with diffusion constant (or viscosity) is relatively small. Hence, experimental inspection might not be very easy.

When the vacuole is large, in the next place, the volume of protoplasm where H^+ can flow becomes smaller. This leads to a decrease in buffer effect such that the fluctuation is absorbed in the medium, making the system remain homogeneous. The homogeneous state can therefore become unstable faster for larger vacuoles, a patterned state can appear. If the vessel containing the extracellular water phase is larger, the fluctuation can be absorbed in the larger buffer medium. This brings the system stably to the homogeneous state. Thus, the smaller volume of water forces the system into a patterned state under illumination.

5. Patterned state

Here, we deal with a description of the banding pattern. A kinetic equation for the H^+ concentration difference across the cell membrane is given first, followed by the derivation of the time-dependent Ginzburg-Landau (TDGL) equation.

5.1. Kinetic equation for H^+-concentration difference

The present model system is composed of diffusion equations valid in the cell exterior and interior for the time-dependent nonlinear boundary condition at the membrane, the external parameter of light intensity being included in the integral constraint on total active flux. In this kind of system, we can obtain the nonlinear differential equation holding at the membrane [9]. The procedure is detailed in appendix C.

Let δn_e and δn_i denote the variance from the homogeneous values N_e and N_i, respectively, then $\delta\Delta n$ can be introduced via

$$\delta\Delta n = \delta n_e - \delta n_i, \tag{19}$$

which is the variance of the H^+-concentration difference across the plasmalemma. The variance of h from the homogeneous state h^0 is introduced using δh. The kinetic equation for $\delta\Delta n$ leads to

$$T\left(\frac{\partial}{\partial t} - D_e\frac{\partial^2}{\partial z^2}\right)\delta\Delta n = J_a(\delta\Delta n,\delta h) + J_p(\delta\Delta n), \tag{20}$$

where T is defined by

$$T = \frac{L}{k\pi}\frac{D_i X_c Y_c}{D_e Y_c Z_c - D_i X_c W_c}, \tag{21}$$

with the definitions of X_c, Y_c, Z_c and W_c by eqs. 16.

The equation for $\delta\Delta h$ is obtained implicitly from the integral constraint of eqs. 4 and 5 as

$$\frac{1}{L}\int_0^L J_a(\delta\Delta n,\delta h)\,\mathrm{d}z = aI. \tag{22}$$

The explicit expression for $J_a(\delta\Delta n,\delta h)$ leads to

$$\begin{aligned} J_a = {} & \frac{\alpha}{1+E} - \frac{\alpha E}{\gamma(1+E)^2}(\delta h - \delta\Delta n) \\ & + \frac{\alpha E(E-1)}{2\gamma^2(1+E)^3}(\delta h - \delta\Delta n)^2 \\ & - \frac{\alpha E(E^2-4E+1)}{6\gamma^3(1+E)^4}(\delta h - \delta\Delta n)^3 \\ & + \frac{\alpha E(E-1)(E^2-10E+1)}{24\gamma^4(1+E)^5}(\delta h - \delta\Delta n)^4 \\ & - \frac{\alpha E(E^4-26E^3+66E^2-26E+1)}{120\gamma^5(1+E)^6} \\ & \times(\delta h - \delta\Delta n)^5 + \cdots, \end{aligned} \tag{23}$$

with E defined by

$$E = \exp\left(\frac{h^0 - \Delta n^0}{\gamma}\right) = \alpha/Ia - 1. \tag{24}$$

The expression for J_p is obviously written as

$$J_p = -p\Delta n^0 - p\delta\Delta n. \tag{25}$$

Eqs. 20 and 22 describe the behavior of $\delta\Delta n$ and δh. Whereas these equations hold only at the

membrane, information on the cell exterior and interior is included in T: this coefficient arises from radial integration within the cell exterior utilizing the flux continuity, which connects the interior to the exterior. The effect of the environment and cytoplasm is also reflected by the threshold light intensity I_c.

5.2. TDGL equation for amplitude of fundamental harmonic

Eq. 20 is a nonlinear differential equation. The boundary condition at the two ends is that of no flux, rewritten from eq. 10 as

$$\frac{\partial}{\partial z}\delta\Delta n = 0 \text{ at } z = 0 \text{ and } L. \tag{26}$$

A formal solution of $\delta\Delta n$ can be expressed as:

$$\delta\Delta n = A_1 \exp\left(i\frac{k\pi}{L}z\right) + A_0 + A_2 \exp\left(i\frac{2k\pi}{L}z\right) + A_3 \exp\left(i\frac{3k\pi}{L}z\right) + \ldots + \text{c.c.}, \tag{27}$$

where c.c. denotes the complex conjugate and k is the integer. The amplitudes, A_l, generally depend on the time t.

Application of a perturbative method presented by Yamafuji et al. [30,31] to eqs. 20 and 22 gives rise to a TDGL equation for A_1. The procedure is very lengthy, and hence is detailed in appendix D. The result is given by

$$T\frac{\mathrm{d}}{\mathrm{d}t}A_1 = \left[\Gamma + GA_1^2 - HA_1^4\right]A_1, \tag{28}$$

where Γ, G and H are expressed by

$$\Gamma = \frac{\alpha(\alpha/Ia - 1)}{\gamma(\alpha/Ia)^2} - \frac{\alpha(\alpha/I_c a - 1)}{\gamma(\alpha/I_c a)^2},$$

$$G = \frac{\alpha^2(\alpha/Ia - 1)^2(\alpha/Ia - 2)^2}{2\gamma^4(\alpha/Ia)^6(U + 2\Gamma)} - \frac{(\alpha/Ia - 1)\left[(\alpha/Ia)^2 - 2\alpha/Ia + 2\right]}{2\gamma^3(\alpha/Ia)^4},$$

$$H = H_c. \tag{29}$$

The expressions for H_c and U are shown in appendix D.

The stationary amplitude of the fundamental harmonic is given by

$$A_{1s}^2 = \left[G \pm \sqrt{G^2 + 4H\Gamma}\right]/2H. \tag{30}$$

The plus sign corresponds to the stable solution with the minus sign denoting unstable. Since the unstable solution exists for $G(I_c) > 0$ referring to an inverted-type bifurcation [30], hysteresis can be observed for one cycle of increased and reduced light intensity. For a relatively wide range of parameter values as used in figs. 3 and 4, the bifurcation belongs to the inverted type. This implies the existence of hysteresis, which agrees with the experimental observation [3].

The pH at the surface can be obtained from superposition of the amplitudes of the first, second, third harmonics, etc. The surface H^+ concentration n_{es} is given by (appendix E)

$$n_{es} = N_e + \sum_{l=1} \frac{A_l}{1 - d_l}\cos(lKz), \tag{31}$$

with d_l and K defined by

$$d_l = D_e Y_c(l) Z_c(l)/D_i X_c(l) W_c(l),$$
$$K = k\pi/L, \tag{32}$$

where $X_c(l)$ is given by a form similar to X_c in eqs. 16 as

$$X_c(l) = K_1(lr_v)I_1(lr_s) - I_1(lr_v)K_1(lr_s), \tag{33}$$

and so on. The physical parameters such as D_i, D_e, R_v and R_r are contained in N_e, A_l and d_l. We can therefore discuss the effect of these parameters on the spatial pattern of $n_{es}(z,t)$. For a description of stationary pH at the surface using eq. 31, it may be sufficient to calculate the terms up to the third harmonics.

The relaxation time $\tau\uparrow$ for the rise of a pattern can be easily obtained from the TDGL equation. As shown in appendix E, $\tau\uparrow$ is given by

$$\tau\uparrow = T/\Gamma. \tag{34a}$$

The relaxation time $\tau\downarrow$ for recovery to the homogeneous state when the light intensity is decreased to I' can be estimated as

$$\tau\downarrow = b/\tau^*(I_c - I'), \tag{34b}$$

where τ^* is given by eq. E6 and b is the numerical coefficient.

5.3. Theoretical results

The analytical results obtained using eqs. 30 and 31 are shown in figs. 5–7 for the effects of D_i, R_v and R_r on the surface pH of alkaline and acidic regions. The results can explain the tendencies of computer simulations. The relation between the pH and D_e is given in fig. 13. These figures show that, while H^+ flow in the protoplasm accelerates alkalinization, the flow does not act favorably in the external aqueous medium. Furthermore, the larger vacuole and smaller reservoir give rise to clearer alkalinization. These facts can also be interpreted as follows: The larger D_i with the smaller D_e makes the spatial pattern evident, and the tiny region where H^+ can flow facilitates alkalinization. This is expressed by

$$D_i \gg D_e, \ (R_r - R_v)/R \ll 1. \tag{35}$$

Fig. 14 illustrates the mechanism of band formation. The H^+ pumps utilize H^+ existing in the protoplasm. If D_i is smaller, a sufficient supply of H^+ to the pumps cannot be guaranteed. If on the other hand, the H^+ flow is rapid in the protoplasm, H^+ from the exterior alkaline regions penetrating into the cell interior can move fluently to the interior side of the acid region, where H^+ pumps demand a supply of H^+. Extruded protons in the acid regions circulate to the alkaline regions in the reservoir. The observed spatial pattern is evident for the smaller diffusion velocity in the cell exterior, as can be intuitively understood. Whereas fast permeation of the cell membrane in the alkaline region is necessary for the completion of the above-mentioned process, the large permeability is really suggested from data on the electric conductance [5,14].

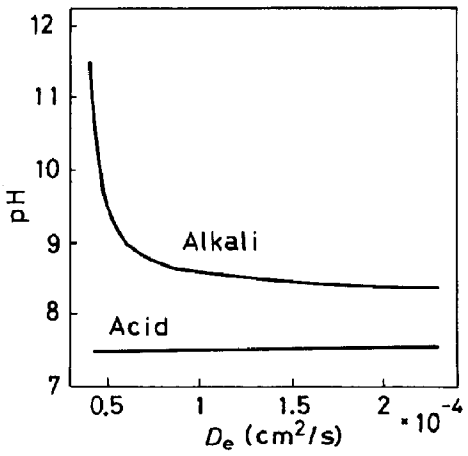

Fig. 13. Dependence of the surface pH values on the diffusion constant D_e. The parameters used in the theoretical analysis follow fig. 7 except for $R_r = 0.75$ mm, $n_\infty = 1.1713 \times 10^{-8}$ M, $\bar{n} = 0.14623$ and D_e changeable.

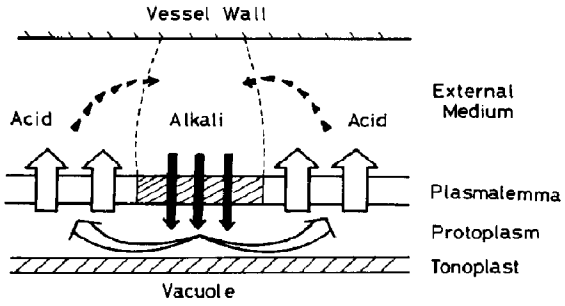

Fig. 14. Intuitive explanation of the mechanism of localized alkalinization and acidification along an internode.

It may be possible to interpret the inequality $D_i \gg D_e$ as implying efflux of OH^- at the alkaline region associated with H^+ efflux at the spatially separated acid region. Diffusion of H^+ along the plasmalemma within the protoplasm is not a rate-limiting process, because OH^- produced through photosynthesis need only be extruded directly at the alkaline region according to the electrochemical gradient. The flow of H^+ and of OH^- constitute equivalent electric current loops.

The effect of the volume of the region where H^+ circulates is also shown in fig. 14. H^+ need not follow a roundabout route to circulate among acid and alkaline zones in the case of the smaller volume. The spatial pattern formed in the narrow space can become more noticeable than that in a wide space.

We next refer to the kinetics of band formation. The analytical results using eqs. 34 are compared in fig. 10 with numerical results. The dependences of the relaxation times on reservoir size display similar tendencies in both the analytical and numerical results. The smaller the reservoir size, the faster the pattern is formed and the more

slowly it decays to recover the homogeneous state. This tendency is also confirmed experimentally [14].

For an intuitive explanation of these phenomena, we present a schematic illustration of the spatial pattern accompanied by H^+ circulation (fig. 15). It takes only a short time during the initial stage for the pattern to arise from a homogeneous state when the reservoir is small due to the short path between the alkaline and acid zones. In contrast, it takes a rather long time in the case of a large vessel, since H^+ takes a roundabout route in order to complete the circulation between these zones. At the later stage, of course, accumulation of H^+ proceeds slowly for a small vessel due to the build-up of a distinct spatial pattern as shown in fig. 7. Fig. 16 demonstrates an example of the numerical results of the rise of the pattern for a very small vessel of $R_r = 0.6$ mm. After the abrupt increase and decrease in H^+ concentration occurring during the initial stage, a slow decrease in the acid region proceeds accompanied by a slow decrease in H^+ in the alkaline region. Fast alkalinization may be inhibited by the extra supply of H^+ from the acid region, differing from the case in fig. 9 with $R_r = 2.5$ mm. Provided that we

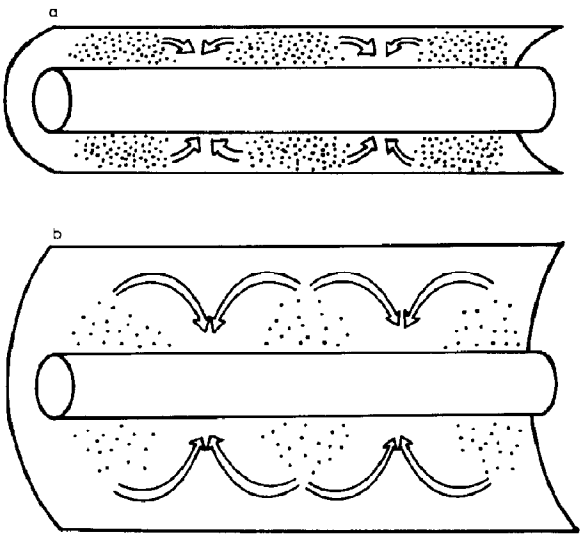

Fig. 15. Circulating electric current and accumulation of H^+ near the surface of an internode placed in the small (a) or large (b) reservoir.

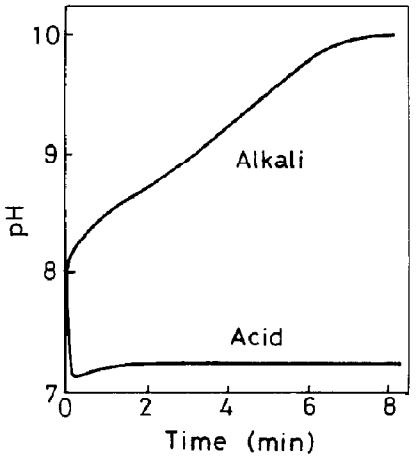

Fig. 16. A numerical example of the time course of the pattern-formation process in a small reservoir of $R_r = 0.6$ mm (cell radius 0.425 mm). The parameters are the same as those in fig. 9.

confine the description to the initial rise of the spatial pattern, however, we can conclude that the pattern is formed more rapidly in the small reservoir due to the short diffusion path than in the large one.

Finally, we provide an explanation for the origin of the slow decay of the pattern in a small vessel. This is brought about by the large accumulation of H^+ in acid zones and depletion in the alkaline zones of the initial pattern. It is confirmed not only by computer simulations as shown in fig. 7 but also by analytical results that the higher harmonics of the spatial mode play dominant roles in the pattern for a small vessel. This situation is also depicted in fig. 15. Thus, such a large degree of accumulation and depletion of H^+ delays the recovery from a patterned state to a homogeneous state.

6. Discussion

The present theoretical model has revealed that Characean banding is a dissipative structure appearing far from equilibrium. It emerges beyond the critical light intensity, as shown in fig. 11. H^+ flow occurs from the acidic region to the alkaline

region in the external aqueous solution, or is associated with OH^- efflux from the alkaline region. Therefore, the change in size of the extracellular water phase can significantly affect such properties of banding as the pH profile and pattern-formation kinetics.

We now consider the mechanism of acid/alkali pattern formation under illumination with the aid of fig. 14. Light induces H^+ efflux through an H^+-electrogenic process along the entire length of the cell. The resultant hyperpolarization and H^+ accumulation at the counter surface (or alkalinization in the protoplasm) cause the subsequent H^+ influx (or OH^- reflux) according to the electrochemical gradient. Although this state, which is uniform along the cell, can be maintained for lower light intensities, a new state can emerge when the light intensity is increased beyond some threshold value: Local small fluctuations can grow to macroscopic spatial orders. This is partly because the membrane permeability to H^+ (or OH^-) increases at high pH [18], as discussed in detail [14]. It should be noted, however, that this autocatalytic process alone cannot produce alternating acid/alkali patterns along the cell. The stabilization of a pattern requires another repressive factor, which limits either the spread of alkalinization due to passive H^+ influx (or OH^- efflux) or that of acidification due to activated H^+ pumps.

Suppose that the membrane permeability happens to increase gradually without attenuation in some local places due to alkalinization occurring initially in the protoplasm as well as subsequent alkalinization in the extracellular water phase, which follows the electrochemical gradient across the membrane. It can then accelerate alkalinization in an autocatalytic manner. This kind of process can generally proceed when the nonlinearity inherent in the system becomes dominant under far-from-equilibrium conditions. However, this process cannot spread over the entire cell length, because the electrogenic H^+ pumps always produce acidification at the cell surface, which acts antagonistically with alkalinization due to passive H^+ (or OH^-) flow through H^+ (or OH^-) channels. Concerning electrogenic H^+ pumps, they cannot all be fully activated along the entire cell length because the energy supply by light is limited, although the pumps may be more activated through photosynthesis utilizing the elevated CO_2 influx in the acid region. We can therefore expect that the acidification process due to H^+ pumps will balance the alkalinization caused by diffusion flux across the membrane; the two regions can separate spatially as shown in fig. 14. The interaction between these regions occurs via the circulating electric current of H^+ and/or OH^-. While the initial formation of an acid/alkali pattern arises in this way, fixation of acid and alkali regions may be related to $CaCO_3$ depositions. The depositions act as nucleation sites for future alkali regions. As the acid/alkali pattern becomes more stabilized under normal conditions day by day, some morphological changes in activated chloroplast distribution and membrane composition might proceed.

The bands in *Chara* are closely analogous to Benard convection, which is a typical dissipative structure appearing far from equilibrium. We can conclude from the theoretical analysis that the acid/alkali banding pattern is also a dissipative structure.

In the present theoretical model, the autocatalytic nature of passive flux is not taken into account explicitly. Incorporation of this autocatalytic nature, however, with the expression for $J_a + J_p$ is mathematically equivalent to the present model including the nonlinearity necessary for pattern formation. By means of this modification, therefore, no major change in qualitative characteristics as a dissipative structure can be expected. Nevertheless, a careful reconsideration of ion species participating in this phenomenon may be required: If OH^- and H^+ are transported autocatalytically across the membrane in the alkaline and acid regions, respectively, we should adopt two kinds of diffusion equations for OH^- and H^+ instead of eq. 1. It may lead to a new situation somewhat different from the present model. While the fundamental properties of dissipative structure mentioned here may be unchanged, a detailed biochemical process might be elucidated more distinctly by the improved approach considering strictly a mechanism of autocatalytic nature. It is also related to the interesting problem of energy coupling at the cellular level. A mathematical modification along this line is a

future task, together with experiments for studying the autocatalytic properties of pH pattern formation.

We must comment on the value of the electric current. The flux given by J_a in fig. 3c amounts to only approx. 0.04 $\mu A/cm^2$, which is much smaller than the observed value of approx. 10 $\mu A/cm^2$. This discrepancy may arise for two reasons. One is that the current is also composed of other ion species than H^+. These ion species may be HCO_3^- and K^+ [6,7]. An H^+ flux of about 1 $\mu A/cm^2$ has been reported under some conditions [1,5,32]. A similar situation occurs in *Fucus* eggs: Although Ca^{2+} can be indispensable in rhizoid formation, Ca^{2+} accounts for only 5% of the total electric current in seawater [33].

The other reason is a possibility that too small a value for α is chosen. Since α in eq. 2 corresponds to the maximum flux, it is better to choose α equal to 5×10^3, much larger than the present value ($= 10$) as one trial if we want to reproduce the flux of 10 $\mu A/cm^2$. Unfortunately, such a large value makes the numerical calculation extremely difficult because of the large difference between α and D_e ($= 0.5$), while the theoretical analysis is possible. Therefore, we adopted this value for the theoretical calculation in fig. 11 so as to express approx. 10 $\mu A/cm^2$. The permeability p was taken as 10^{-3} cm/s ($= 0.25$), which has been reported experimentally [32]. Whereas we also performed a theoretical calculation using the parameter values adopted in the numerical results in fig. 3, a result similar to that in fig. 11 was obtained. Thus, the essential properties demonstrated by a dissipative structure cannot be changed by the magnitude of the electric current.

It should be noted, however, that the usual estimate of an electric current from the voltage difference becomes misleading in some cases. Since the electric current originates in the electrochemical-potential gradient, the diffusion flux due to the concentration difference must be taken into account. Therefore, careful reconsideration may be necessary for the experimentally estimated value of an electric current.

As mentioned in a recent observation [14], the rise in spatial pattern from the homogeneous state usually takes several minutes. The corresponding result in the theory shown in fig. 10a gives a relaxation time of 1 min or so, which is faster than that observed. This may be because our theory disregards the activation time of the photosynthetic process in chloroplasts under illumination. In fact, eq. 5 implies that the active flux is elicited in a straightforward manner when illumination is imposed. Incorporation of the temporal relationship between light intensity and active flux into the theory could be relatively simple provided that one is permitted to do so in a phenomenological fashion. This procedure remains a future task.

The critical light intensity, above which spatial inhomogeneity appears, has been shown to depend on the viscosity of the aqueous solution and size of the vessel (see fig. 12). However, these changes are relatively small, and hence rather minute measurements might be necessary for experimental inspection.

It is necessary to study the electric characteristics of a particularly conditioned internode, which exhibits no band at pH approx. 8, by intensionally choosing an adequate medium; under the usual conditions using artificial pond water at pH 8 bands are observed, and a low electric resistance along the cell occurs at extremely high pH [14,18]. If a high electric resistance should be observed at a higher pH of about 11 contrary to the normal internode, it might be considered that there is a strong possibility that the alkali-induced permeability change plays a dominant role in the bands.

Pattern formation is a typical nonlinear, nonequilibrium phenomenon. The temporal oscillation also belongs to the category of self-organized phenomena appearing far from equilibrium. Characean internodes show self-oscillation of the membrane potential [34,35]. This indicates the inherence of the positive-feedback loop in chemical and physical processes occurring in the cell. A similar oscillation has been observed in a *Nitella* protoplasmic droplet [36], and has been explained theoretically [37]. We can suppose that the spatial pattern as well as the temporal oscillation arise from the same positive-feedback origin. In other words, these two phenomena should not be studied separately but should be treated within a broader biophysical framework, i.e., as a spatio-temporal organization.

Appendix A

Nondimensional quantities are obtained by defining n_∞, $\tilde{n}$, $\tilde{R}$ and $\tilde{\tau}$ as the quantities related to the external H^+ concentration, those giving the order to the cell radius and the H^+ diffusion time, respectively. The right-hand sides refer to the nondimensional terms:

$$n/n_\infty + \tilde{n} \to n,\ r/\tilde{R} \to r,\ z/\tilde{R} \to z,\ t/\tilde{\tau} \to t,$$
$$h/n_\infty \to h,$$
$$R/\tilde{R} \to R,\ R_v/\tilde{R} \to R_v,\ R_r/\tilde{R} \to R_r,\ L/\tilde{R} \to L,$$
$$(\tilde{\tau}/\tilde{R}n_\infty)\alpha \to \alpha,\ (\tilde{\tau}/\tilde{R})p \to p,\ (\tilde{\tau}/\tilde{R}^2)D_{e,i} \to D_{e,i}, \quad \text{(A1)}$$

with $D_{e,i}$ denoting D_e and D_i. We have chosen $\tilde{R} = 0.5$ mm and $\tilde{\tau} = 12.5$ s; values of n_∞ and $\tilde{n}$ are listed in each figure legend. Since R is set at 0.85, the radius amounts to 0.425 mm, in good agreement with the real radius of an internode.

Appendix B

The small quantities δn_e, δn_i and δh are introduced via

$$n = \begin{cases} N_e + \delta n_e & \text{at} \quad R < r < R_r, \\ N_i + \delta n_i & \text{at} \quad R_v < r < R, \end{cases}$$
$$h = h^0 + \delta h. \quad \text{(B1)}$$

The diffusion equations can be rewritten as

$$\frac{\partial}{\partial t}\delta n_{e,i} = D_{e,i}\left[\frac{1}{r}\frac{\partial}{\partial r}\left(r\frac{\partial}{\partial r}\right) + \frac{\partial^2}{\partial z^2}\right]\delta n_{e,i}, \quad \text{(B2)}$$

with $\delta n_{e,i}$ designating δn_e and δn_i. The boundary conditions are reduced to

$$\frac{\partial}{\partial r}\delta n_i = 0 \quad \text{at } r = R_v,$$
$$\frac{\partial}{\partial r}\delta n_e = 0 \quad \text{at } r = R_r,$$
$$\frac{\partial}{\partial z}\delta n_{e,i} = 0 \quad \text{at } z = 0 \text{ and } L. \quad \text{(B3)}$$

The solution of eq. B2 under the condition, eq. B3 can be expressed by

$$\delta n_e = \sum_k \left[\hat{A}_k K_0\left(\frac{\beta_k}{\sqrt{D_e}}r\right) + B_k I_0\left(\frac{\beta_k}{\sqrt{D_e}}r\right)\right] \times \cos\left(\frac{k\pi}{L}z\right)\exp(-\lambda_k^2 t),$$
$$\delta n_i = \sum_k \left[C_k K_0\left(\frac{\beta_k'}{\sqrt{D_i}}r\right) + D_k I_0\left(\frac{\beta_k'}{\sqrt{D_i}}r\right)\right] \times \cos\left(\frac{k\pi}{L}z\right)\exp(-\lambda_k^2 t), \quad \text{(B4)}$$

where K_ν and I_ν are modified Bessel functions of the ν-th order. The relationships among β_k, β_k' and λ_k are

$$\beta_k^2 = D_e\left(\frac{k\pi}{L}\right)^2 - \lambda_k^2,\ \beta_k'^2 = D_i\left(\frac{k\pi}{L}\right)^2 - \lambda_k^2, \quad \text{(B5)}$$

or

$$\beta_k'^2 = \beta_k^2 + (D_i - D_e)\left(\frac{k\pi}{L}\right)^2. \quad \text{(B6)}$$

The expansion coefficients $\hat{A}_k$, B_k, C_k and D_k can be determined from eqs. 4 and 5 under the condition of eq. 7. Substitution of eqs. B1 and B4 into eqs. 4 and 5 leads to

$$\delta h = 0. \quad \text{(A7)}$$

The flux continuity is rewritten as

$$-D_e\left(\frac{\partial \delta n_e}{\partial r}\right)_s = -D_i\left(\frac{\partial \delta n_i}{\partial r}\right)_s = \left[-p + \frac{\alpha(\alpha/Ia - 1)}{\gamma(\alpha/Ia)^2}\right] \times (\delta n_{es} - \delta n_{is}). \quad \text{(B8)}$$

Putting eqs. B4 into eqs. B3 and B8 we then obtain:

$$B_k = \frac{K_1(x_r)}{I_1(x_r)},$$
$$C_k = \frac{\sqrt{D_e}\beta_k I_1(x_v)}{\sqrt{D_i}\beta_k' I_1(x_r)} \times \frac{K_1(x_r)I_1(x_s) - I_1(x_r)K_1(x_s)}{K_1(x_v)I_1(x_s') - I_1(x_v)K_1(x_s')},$$

$$D_k = \frac{K_1(x_v)}{I_1(x_v)} C_k, \tag{B9}$$

where x_r, x_v, x_s and x_s' are defined by

$$x_r = \frac{\beta_k}{\sqrt{D_e}} R_r,\ x_v = \frac{\beta_k'}{\sqrt{D_i}} R_v,\ x_s = \frac{\beta_k}{\sqrt{D_e}} R,$$

$$x_s' = \frac{\beta_k'}{\sqrt{D_i}} R. \tag{B10}$$

In the expressions for B_k, C_k and D_k we put $\hat{A}_k$ as being equal to unity.

If we substitute eqs. B4 with eqs. B9 into eqs. B8, we have

$$-p + \frac{\alpha(\alpha/Ia - 1)}{\gamma(\alpha/Ia)^2} = \frac{\sqrt{D_e D_i}\,\beta_k \beta_k' XY}{\sqrt{D_e}\,\beta_k YZ - \sqrt{D_i}\,\beta_k' XW}, \tag{B11}$$

with X, Y, Z and W defined by

$$X = K_1(x_v) I_1(x_s') - I_1(x_v) K_1(x_s'),$$
$$Y = K_1(x_r) I_1(x_s) - I_1(x_r) K_1(x_s),$$
$$Z = K_1(x_v) I_0(x_s') + I_1(x_v) K_0(x_s'),$$
$$W = K_1(x_r) I_0(x_s) + I_1(x_r) K_0(x_s). \tag{B12}$$

Since β_k' is related to β_k by eq. B6 and β_k is expressed by λ_k through eq. B5, the resultant eq. B11 gives λ_k as a function of I, D_e, R_r, etc.

From eqs. B4, the small variances will decay when λ_k^2 takes positive values. This means the homogeneous-flux state exists stably under thermal fluctuations. If λ_k^2 becomes negative, on the other hand, small variations can grow. The homogeneous state can no longer remain stable, and hence a spatial mode can develop. Thus, the stability change occurs at $\lambda_k = 0$. Fig. 11 shows that the homogeneous state becomes unstable to bring about the spatial pattern above some threshold value I_c of light intensity, which corresponds to $\lambda_k = 0$. Eq. B11 gives I_c by putting $\lambda_k = 0$ as in eq. 15.

Appendix C

The diffusion equations for δn_e and δn_i are given by eq. B2. The formal solutions for the fundamental harmonic of mode k are therefore written as

$$\delta n_e = \left[\hat{A}_k K_0\left(\frac{\beta_k}{\sqrt{D_e}} r\right) + B_k I_0\left(\frac{\beta_k}{\sqrt{D_e}} r\right)\right] N(z,t), \tag{C1a}$$

$$\delta n_i = \left[C_k K_0\left(\frac{\beta_k'}{\sqrt{D_i}} r\right) + D_k I_0\left(\frac{\beta_k'}{\sqrt{D_i}} r\right)\right] N(z,t). \tag{C1b}$$

If we substitute eq. C1a into eq. B2 and then integrate the resulting equation by multiplying r with respect to r, we obtain

$$-D_e\left(r\frac{\partial \delta n_e}{\partial r}\right)_s = \frac{\sqrt{D_e}}{\beta_k} R\left[\hat{A}_k K_1\left(\frac{\beta_k}{\sqrt{D_e}} R\right) - B_k I_1\left(\frac{\beta_k}{\sqrt{D_e}} R\right)\right] \times\left(\frac{\partial}{\partial t} - D_e\frac{\partial^2}{\partial z^2}\right) N. \tag{C2}$$

By using eq. B9 the diffusion flux at the membrane is rewritten as

$$-D_e\left(\frac{\partial \delta n_e}{\partial r}\right)_s = \frac{\sqrt{D_e}}{\beta_k} \frac{Y}{I_1\left(\frac{\beta_k}{\sqrt{D_e}} R_r\right)} \times\left(\frac{\partial}{\partial t} - D_e\frac{\partial^2}{\partial z^2}\right) N. \tag{C3}$$

The variance of Δn, $\delta\Delta n$, can be related to N as

$$\delta\Delta n = \delta n_e - \delta n_i = \left[\hat{A}_k K_0\left(\frac{\beta_k}{\sqrt{D_e}} R\right) + B_k I_0\left(\frac{\beta_k}{\sqrt{D_e}} R\right) - C_k K_0\left(\frac{\beta_k'}{\sqrt{D_i}} R\right) - D_k I_0\left(\frac{\beta_k'}{\sqrt{D_i}} R\right)\right] N. \tag{C4}$$

Putting eqs. B9 into eq. C4 we then obtain

$$N(z,t) = \frac{\sqrt{D_i}\beta_k' I_1\left(\frac{\beta_k}{\sqrt{D_e}} R_r\right) X}{\sqrt{D_i}\beta_k' XW - \sqrt{D_e}\beta_k YZ} \delta\Delta n. \quad \text{(C5)}$$

The diffusion flux at the membrane becomes

$$-D_e\left(\frac{\partial \delta n_e}{\partial r}\right)_s = \frac{\beta_k'}{\beta_k} \frac{\sqrt{D_e D_i}\, XY}{\sqrt{D_e}\, YZ - \sqrt{D_i}\, XW} \times \left(\frac{\partial}{\partial t} - D_e \frac{\partial^2}{\partial z^2}\right) \delta\Delta n. \quad \text{(C6)}$$

We approximate the coefficient of the right-hand side of eq. C6 by the value at the critical point I_c; it implies $\lambda_k = 0$. Substitution of the resulting expression into the flux continuity leads to eq. 20.

Appendix D

The basic procedure used here is from the previously described method [9,30]. We choose the stationary amplitude of the first harmonic w ($= A_{1s}$) as a small expansion parameter. While any selection of other small parameters may be possible, the physical meaning is clear in this case [18,31]. The bifurcation parameter I can be expanded as

$$I = I_c + \mu b_1 w^2 - b_2 w^2 + \cdots, \quad \text{(D1)}$$

where μ is the sign factor with $+1$ the supercritical and -1 the subcritical. The coefficients b_1 and b_2 are determined from the stationary condition of the equations obtained for the w^3-th and w^5-th orders, respectively. The expansion of eq. D1 is somewhat analogous to bifurcation theory [18]. Although bifurcation theory treats only the stationary state, the present method can also discuss the kinetics.

When $\delta\Delta n$ is expanded as the Fourier series of eq. 27, A_1 can be expressed by

$$A_1 = wW(T_1, T_2, \cdots) \quad \text{(D2)}$$

and the other coefficients are formally expanded as [30]

$$A_0 = w^2 W_{00} + w^4 W_{02} + \cdots,$$
$$A_2 = w^2 W_{20} + w^4 W_{22} + \cdots,$$
$$A_3 = w^3 W_{30} + w^5 W_{32} + \cdots, \quad \text{(D3)}$$

and so on. The amplitude W depends on such a slow time scale as T_1, and is reduced to unity at the stationary state.

The scale transformations of time and space are made:

$$\frac{\partial}{\partial t} = w^2 \frac{\partial}{\partial T_1} + w^4 \frac{\partial}{\partial T_2} + \cdots,$$
$$\frac{\partial^2}{\partial z^2} = -l^2\left(\frac{k\pi}{L}\right)^2. \quad \text{(D4)}$$

Furthermore we must expand δh as

$$\delta h = w^2 h_1 + w^4 h_2 + \cdots. \quad \text{(D5)}$$

Substituting eqs. D1–D5 into eqs. 20 and 22, we obtain eq. 15 for the w-th order. The second-order balance equation gives rise to

$$W_{00} = 0,$$
$$W_{20} = \frac{\alpha(\hat{\alpha}-1)(\hat{\alpha}-2)}{6\gamma^2\hat{\alpha}^3 P} W^2 \equiv a_2 W^2,$$
$$h_1 - \frac{\hat{\alpha}-2}{\gamma\hat{\alpha}} W^2, \quad \text{(D6)}$$

where $\hat{\alpha}$ and P are given by

$$\hat{\alpha} = \alpha/I_c a, \; P = -p + \frac{\alpha(\hat{\alpha}-1)}{\gamma\hat{\alpha}^2}. \quad \text{(D7)}$$

The solvability condition for the third-order balance equation leads to the TDGL equation for W:

$$T\frac{\partial}{\partial T_1} W = \left[\frac{a(\alpha - 2aI_c)\mu b_1}{\gamma a} + G_c W^2\right] W, \quad \text{(D8)}$$

where G_c is given by

$$G_c = \frac{\alpha(\hat{\alpha}-1)(\hat{\alpha}-2)}{\gamma^2\hat{\alpha}^3} a_2 - \frac{\alpha(\hat{\alpha}-1)(\hat{\alpha}^2 - 2\hat{\alpha} + 2)}{2\gamma^3\hat{\alpha}^4}. \quad \text{(D9)}$$

The stationary condition of $\partial/\partial T_1 = 0$ and $W = 1$

gives

$$\mu b_1 = -\frac{\gamma\alpha G_c}{a(\alpha - 2aI_c)}. \tag{D10}$$

The coefficient W_{30} for the third harmonic is

$$W_{30} = \frac{\alpha(\hat{\alpha}-1)}{8\gamma^2\hat{\alpha}^3 P}\left[(\hat{\alpha}-2)a_2 + \frac{\hat{\alpha}^2 - 6\hat{\alpha} + 6}{6\gamma\hat{\alpha}}\right]W^3$$
$$\equiv a_3 W^3. \tag{D11}$$

The fourth-order balance equation produces expressions for W_{02}, W_{22}, W_{40} and h_2. Since they are very lengthy, we will not show them explicitly but proceed further.

Finally, the solvability condition of the fifth-order balance equation gives

$$T\frac{\partial}{\partial T_2}W = \left\{\frac{a}{\gamma\alpha}\left[2ab_2 I_c - \alpha b_2 - a(\mu b_1)^2\right] + \mu G_c' W^2 - H_c W^4\right\}W, \tag{D12}$$

where G_c' and H_c have the forms of

$$G_c' = \frac{a(\alpha^2 - 6\alpha a I_c + 6a^2 I_c)b_1 a_2}{\gamma^2\alpha^2} - \frac{a(\alpha - aI_c)^3 b_1}{2\gamma^3\alpha^3} - \frac{(\hat{\alpha}-1)(\hat{\alpha}-2)ab_1}{6\gamma^4\alpha\hat{\alpha}^3 P}\left[2\gamma\alpha(\alpha - 2aI_c)a_2 - (\alpha^2 - 6\alpha a I_c + 6a^2 I_c^2)\right], \tag{D13a}$$

and

$$H_c = \frac{\alpha(\hat{\alpha}-1)}{\gamma^2\hat{\alpha}^3}\left[\frac{2(\hat{\alpha}-1)a_2^2}{\gamma\hat{\alpha}} - (\hat{\alpha}-2)(a_2 a_3 + \hat{a}_2) + \frac{4(\hat{\alpha}-2)(\hat{\alpha}^2 - 3\hat{\alpha} + 3)a_2}{3\gamma^2\hat{\alpha}^2} - \frac{(\hat{\alpha}^2 - 6\hat{\alpha} + 6)a_3}{2\gamma\hat{\alpha}} - \frac{(2\hat{\alpha}^4 - 9\hat{\alpha}^3 + 21\hat{\alpha}^2 - 24\hat{\alpha} + 12)}{6\gamma^3\hat{\alpha}^3} + \frac{2(\hat{\alpha}-2)a_2 G_c}{3P}\right], \tag{D13b}$$

with

$$\hat{a}^2 = \frac{\alpha(\hat{\alpha}-1)}{3\gamma^2\hat{\alpha}^3 P}\left[(\hat{\alpha}-2)a_3 - \frac{2(\hat{\alpha}-1)a_2}{\gamma\hat{\alpha}} - \frac{(\hat{\alpha}-2)(\hat{\alpha}^2 - 3\hat{\alpha} + 3)}{3\gamma^2\hat{\alpha}^2}\right]. \tag{D14}$$

For $\partial/\partial T_2 = 0$ and $W = 1$, we obtain

$$b_2 = -\frac{\gamma\alpha}{a(\alpha - 2aI_c)}(H_c - \mu G_c') - \frac{\gamma^2\alpha^2}{a(\alpha - 2aI_c)^3}G_c^2. \tag{D15}$$

If we introduce Γ, G and H by

$$\Gamma = \frac{a(\alpha - 2aI_c)\mu b_1}{\gamma\alpha}w^2 + \frac{a\left[2ab_2 I_c - \alpha b_2 - a(\mu b_1)^2\right]}{\gamma\alpha}w^4,$$
$$G = G_c + G_c'\mu w^2,$$
$$H = H_c, \tag{D16}$$

we arrive at eq. 28. The summed-up expressions for Γ, G and H are given by eqs. 29.

We can easily check that eq. D1 with eqs. D9 and D15 becomes the same as the stationary equation of eq. 28.

While for $G_c > 0$ the bifurcation is of the inverted type, the inequality of $G_c < 0$ gives normal-type bifurcation, as shown in fig. 17. The

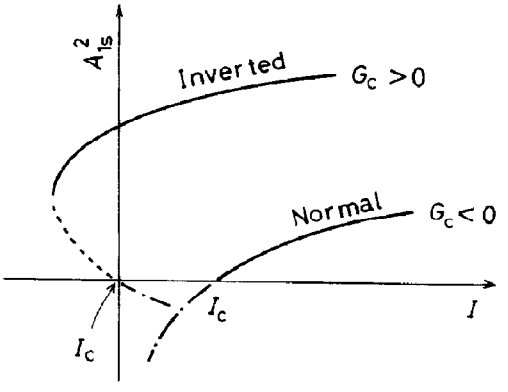

Fig. 17. Normal-type and inverted-type bifurcations.

present model system exhibits interesting behavior: The type of bifurcation changes according to the size of the reservoir (fig. 18). As the reservoir becomes smaller, the bifurcation tends to become inverted. This is presumably related to the enhancement of nonlinearity brought about by the decrease in volume where H^+ can flow.

The summed-up expressions for A_2 and A_3 are

$$A_2 = \left\{ \frac{\alpha(\alpha/Ia-1)(\alpha/Ia-2)}{2\gamma^2(\alpha/Ia)^3\left(U+T\frac{\mathrm{d}}{\mathrm{d}t}\right)} + \hat{a}_2 A_1^2 \right\} A_1^2,$$

$$A_3 = \left\{ \frac{\alpha(\alpha/Ia-1)}{6\gamma^3(\alpha/Ia)^4 F} \left[\frac{3\alpha(\alpha/Ia-1)(\alpha/Ia-2)^2}{\gamma(\alpha/Ia)^2\left(U+\frac{2T}{3}\frac{\mathrm{d}}{\mathrm{d}t}\right)} + (\alpha/Ia)^2 - 6(\alpha/Ia) + 6 \right] + \hat{a}_3 A_1^2 \right\} A_1^3, \tag{D17}$$

with U and F defined by

$$U = 4\left(\frac{k\pi}{L}\right)^2 D_e T + p - \frac{\alpha(\alpha/Ia-1)}{\gamma(\alpha/Ia)^2},$$

$$F = 9\left(\frac{k\pi}{L}\right)^2 D_e T + p - \frac{\alpha(\alpha/Ia-1)}{\gamma(\alpha/Ia)^2} + T\frac{\mathrm{d}}{\mathrm{d}t}. \tag{D18}$$

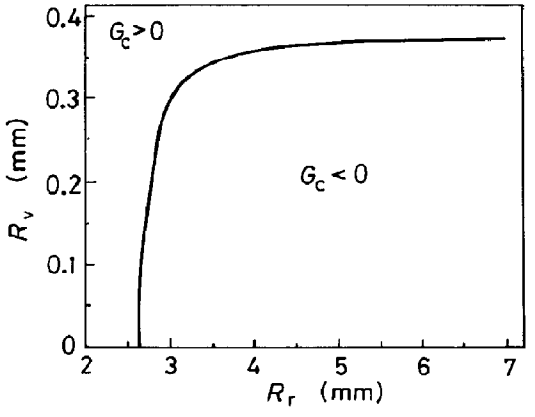

Fig. 18. Phase diagram of normal-type and inverted-type bifurcations on the plane of R_v and R_r. Parameters are the same as those in fig. 12.

An expression for $\hat{a}_3$ is omitted here due to the tediousness.

Appendix E

To determine the surface H^+ concentration, we must establish the relation between δn_{es} and $\delta\Delta n$ for each harmonic. From eqs. C1 with eq. B9, δn_{is} is related to δn_{es} by

$$\delta n_{is} = \frac{\sqrt{D_e}\beta_k YZ}{\sqrt{D_i}\beta_k' XW}\delta n_{es}. \tag{E1}$$

Near the bifurcation point, we can approximate

$$\delta n_{is} = \frac{D_e Y_c Z_c}{D_i X_c W_c}\delta n_{es}. \tag{E2}$$

Thus, δn_{es} for the l-th harmonic is given by $\delta\Delta n$ with eq. 19 as

$$\delta n_{es} = \frac{\delta\Delta n}{1-d_l}. \tag{E3}$$

with d_l being given by eq. 32. The surface H^+ concentration is obtained by summing up each harmonic. The result corresponds to eq. 31.

The relaxation time $\tau\uparrow$ for the rise of a pattern can be estimated by linearizing the TDGL equation, eq. 28, around the homogeneous state. Let f be the small variance, then eq. 28 becomes

$$T\frac{\mathrm{d}}{\mathrm{d}t}f = \Gamma f. \tag{E4}$$

In this equation, $\tau\uparrow$ is given by eq. 34a.

As for the relaxation time $\tau\downarrow$, we estimate the kinetics from the patterned to the homogeneous state as those around the patterned state chosen under the initial condition. This is because the present TDGL equation cannot apply to a situation far from the bifurcation point. Furthermore, the results shown in fig. 10b may be considered as reflecting the stability of a patterned state chosen at the initial time. Thus, the above estimate becomes only qualitative but is a good tentative explanation of the relaxation time.

Substituting $A_1 = A_{1s} + f$ into eq. 28, we obtain

$$T\frac{\mathrm{d}}{\mathrm{d}t}f = -2\sqrt{G^2 + 4H\Gamma}A_{1s}^2 f. \tag{E5}$$

The relaxation time τ^* for f can be easily obtained as

$$\tau^* = T/2\sqrt{G^2 + 4H\Gamma}\,A_{1s}^2. \quad \text{(E6)}$$

For smaller values of τ^*, the patterned state is rather stable because the system recovers rapidly to the initial patterned state even after a disturbance. When the light intensity is decreased to I', the driving force to shift the system to a homogeneous state may be roughly estimated as $I_c - I'$. Relaxation to the homogeneous state can be considered as fast for the weakly stable initial patterned state under a strong driving force. Therefore, the relaxation time $\tau\downarrow$ is inversely proportional to τ^* and $I_c - I'$, as given by eq. 34b.

References

1 D.G. Spear, J.K. Barr and C.E. Barr, J. Gen. Physiol. 54 (1969) 397.
2 N.A. Walker and F.A. Smith, J. Exp. Bot. 28 (1977) 1190.
3 W.J. Lucas, J. Exp. Bot. 26 (1975) 347.
4 K. Ogata, Plant Cell Physiol. 24 (1983) 695.
5 K. Ogata, T.C. Chilcott and H.G.L. Coster, Aust. J. Plant Physiol. 10 (1983) 339.
6 F.A. Smith and N.A. Walker, J. Exp. Bot. 31 (1980) 119.
7 W.J. Lucas and J. Dainty, J. Membrane Biol. 32 (1977) 75.
8 K. Toko, H. Chosa and K. Yamafuji, J. Theor. Biol. 114 (1985) 127.
9 K. Toko, S. Iiyama and K. Yamafuji, J. Phys. Soc. Jap. 53 (1984) 4070.
10 K. Toko and K. Yamafuji, in: The theory of dynamical systems and its applications to nonlinear problems, ed. H. Kawakami (World Sci., Singapore, 1984) p. 228.
11 P. Gransdorff and I. Prigogine, Thermodynamic theory of structure, stability and fluctuations (Wiley-Interscience, London, 1971).
12 S. Iiyama, K. Toko and K. Yamafuji, Biophys. Chem. 21 (1985) 285.
13 M. Paques, C. Sironval and S. Bonotto, in: Developmental biology of *Acetabularia*, eds. S. Bonotto, V. Kefeli and S. Puiseux-Dao (Elsevier/North-Holland, Amsterdam, 1979) p. 155.
14 K. Ogata, K. Toko, T. Fujiyoshi and K. Yamafuji, Biophys. Chem. 26 (1987) 71.
15 J.M. Ferrier, J. Theor. Biol. 85 (1980) 739.
16 N.A. Walker, F.A. Smith and I.R. Cathers, J. Membrane Biol. 57 (1980) 51.
17 P.T. Smith and N.A. Walker, J. Membrane Biol. 60 (1981) 223.
18 M.A. Bisson and N.A. Walker, J. Membrane Biol. 56 (1980) 1.
19 P. Matile, Annu. Rev. Plant Physiol. 29 (1978) 193.
20 H. Meinhardt, Models of biological pattern formation (Academic Press, London, 1982)
21 R. Blumenthal, J. Theor. Biol. 49 (1975) 219.
22 D.W. Peaceman and H.H. Rachford, J. Soc. Ind. Appl. Math. 3 (1955) 28.
23 W.J. Lucas and R. Nuccitelli, Planta 150 (1980) 120.
24 K. Toko and K. Yamafuji. J. Phys. Soc. Jap. 51 (1982) 3049.
25 W.J. Lucas and T. Shimmen, J. Membrane Biol. 58 (1981) 227.
26 K. Toko and K. Yamafuji, Biophys. Chem. 14 (1981) 11.
27 T.L. Hill, Introduction to statistical thermodynamics (Addison-Wesley, Reading, MA, 1960).
28 T.C. Chilcott, H.G.L. Coster, K. Ogata and J.R. Smith, Aust. J. Plant Physiol. 10 (1983) 353.
29 A. Dorn and M.H. Weisenseel, J. Exp. Bot. 35 (1984) 373.
30 K. Yamafuji, K. Toko and K. Urahama, J. Phys. Soc. Jap. 50 (1981) 3819.
31 K. Toko, J. Nitta, K. Urahama and K. Yamafuji, Electr. Commun. Jap. 64A (9) (1981) 1.
32 H. Kitasato, J. Gen. Physiol. 52 (1968) 60.
33 R. Nuccitelli and L.F. Jaffe, J. Cell Biol. 64 (1975) 636.
34 K. Ogata and U. Kishimoto, Plant Cell Physiol. 17 (1976) 201.
35 H.D. Boels and U.P. Hansen, Plant Cell Physiol. 23 (1982) 343.
36 Y. Kobatake, I. Inoue and T. Ueda, Adv. Biophys. 7 (1975) 43.
37 K. Toko, M. Nosaka, M. Tsukiji and K. Yamafuji, Biophys. Chem. 21 (1985) 295.